frontiers | Frontiers in Astronomy and Space Sciences

TYPE Original Research
PUBLISHED 11 May 2023
DOI 10.3389/fspas.2023.1146705

OPEN ACCESS

EDITED BY
Sergei M. Kopeikin,
University of Missouri, United States

REVIEWED BY
Louis Neal Irwin,
The University of Texas at El Paso, United States
Antonio Genova,
Sapienza University of Rome, Italy

*CORRESPONDENCE
Troy Shinbrot,
shinbrot@rutgers.edu

RECEIVED 17 January 2023
ACCEPTED 17 April 2023
PUBLISHED 11 May 2023

CITATION
Shinbrot T (2023), Gravitational influence of Saturn's rings on its moons: a case for free granular flow.
Front. Astron. Space Sci. 10:1146705.
doi: 10.3389/fspas.2023.1146705

Gravitational influence of Saturn's rings on its moons: a case for free granular flow

Troy Shinbrot*

Department of Physics and Astronomy, Rutgers University, Piscataway, NJ, United States

Exploratory missions have found that regolith on interplanetary bodies can be loosely packed and freely flowing—a state that strongly affects mission plans and that may also influence the large-scale shapes of these bodies. We investigate here whether notable circumferential ridges seen on Saturn's moons may be a byproduct of free flow of loosely packed regolith. Such ridges and other features likely record the history of the moons, and we find that if surface grains are freely flowing, then the combined gravity of Saturn itself and its tenuous ring generate similar circumferential features. Moreover, analysis of these features reveals the possibility of previously unreported morphologies, for example, a stationary torus around a non-rotating satellite. Some of these features persist even for a very low density and distant disk, which raises the prospect that nonlinear analysis of interactions from disks to moons and back again may lead to new insights.

KEYWORDS

Saturn, moons in the Solar system, gravitational model, granular flow, nonlinear analysis

Introduction

International exploratory missions have visited interplanetary bodies and have found their regolith to be loosely packed and freely flowing (Thomas et al., 2015; Lauretta et al., 2017). These findings concur with both modeling (Meakin et al., 1986) and terrestrial experiments (Shinbrot et al., 2004; Shinbrot et al., 2017) intended to investigate how the processes of fine scale regolith accretion produce larger scale morphogenesis. Nowhere is this morphogenesis more striking than on Saturn's moons, which exhibit remarkable equatorial features, some of which are shown in Figure 1. Pan and Atlas (Figures 1A,B) have such prominent equatorial ridges that the moons resemble ravioli, with aspect ratios around ½. Iapetus (Figure 1C) is much larger and is nearly spherical, but has a sharp, 20 km high, ridge over most of its circumference. By contrast, the asteroid Vesta (Figure 1D) is scoured by multiple, 2 km deep, troughs extending along much of its equator.

The origins of these features are unknown. Theories for the formation of equatorial ridges include collisions between matched pairs of bodies (Leleu et al., 2018), viscous deformation of ring material (Charnoz et al., 2011), and accretion of material from a flat ring onto a central satellite (Charnoz et al., 2007; Porco et al., 2007). No existing theory predicts equatorial troughs. We show here that troughs as well as ridges arise naturally if freely flowing grains follow equipotentials of a massive spheroid in a massive plane, as shown in Figures 1E–H). This possibility does not appear to have been examined previously.

The binary collision theory produces veridical equatorial ridges (Leleu et al., 2018), but requires that the two bodies have nearly identical masses, and deform rather than fragment. Additionally, constraints on the collision impact parameter are stringent, both so that the bodies aren't torn apart by centrifugal forces and because any nonzero impact parameter would

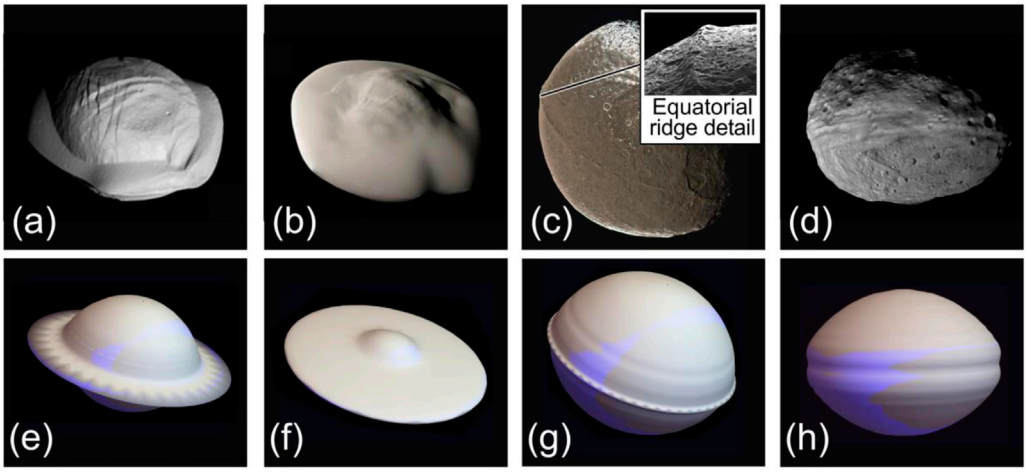

FIGURE 1
(A–D) Saturn's moons Pan, Atlas and Iapetus, and the asteroid Vesta (credit NASA/JPL-Caltech/SSI) compared with simulations **(E–H)** of morphology expected for freely flowing grains on a spheroidal mass influenced by a thin, weakly gravitational plane. Simulation parameters (defined in text): **(E)** $\omega = 5.15, R_{excised} = 4R_{moon}, R_{polar} = 0.85R_{moon}, \rho_{plane} = \rho_{moon}$; **(F)** same as panel **(E)** but with $\rho_{plane} = 1.2\rho_{moon}$, **(G)** $\omega = 8, R_{excised} = 3.2\,R_{moon}, \rho_{plane} = \rho_{moon}$; **(H)** $\omega = 25, R_{excised} = 2.5\,R_{moon}, \rho_{plane} = \rho_{moon}$. Geometry of simulations is shown in Figure 2C, where plane thickness is 2% of spheroid's major axis and plane outer radius is 10 times the radius of the moon in these panels.

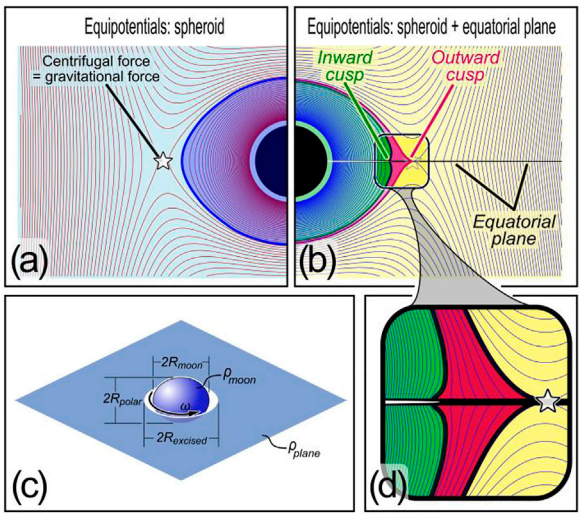

FIGURE 2
Gravitational equipotentials. **(A)** Equipotentials of central sphere (black) rotating with speed $\omega = 15$. **(B)** Equipotentials of the same sphere embedded in a plane whose density is half that of the central sphere, using the geometry shown in **(C)**. **(D)** Enlargement of region near equator, highlighting both an inward and outward cusp. Equipotentials in **(B)** and **(D)** are for outer diameter of the plane $10R_{moon}$, plane thickness $0.02R_{moon}$, and where a radius $R_{excised} = 2.8R_{moon}$ of mass is removed from the plane as described in text.

produce rotation perpendicular to the moons' equators—opposite of their current orientations. Moreover Pan and Atlas, and possibly Pandora and Daphnis as well, are quite similar in shape, making for an impressive coincidence of remarkable events.

The theories of ridge formation from ring material, on the other hand, involve highly probable mechanisms such as viscous spreading early in a moon's evolution (Charnoz et al., 2011) and deposition of ring material onto a satellite later (Charnoz et al., 2007; Porco et al., 2007). The deposition model is supported by data from close fly-bys indicating that Pan, Atlas and other smaller moons are likely composed of a high density core surrounded by much lower density accreted material (Buratti et al., 2019). To date, however, deposition models have not reproduced the curious shapes shown in Figure 1.

Gravitational equipotentials

Both types of theory are based on the presumption that equatorial features require a secondary morphogenetic process—collision, viscous spreading, or accretion—because equatorial features are not predicted from simple gravitational and inertial considerations. That is, as shown in cross section in Figure 2A, equipotentials of a rotating spheroid are themselves nearly spheroidal (for example, in the blue cross section shown), and lack equatorial ridges or grooves. On the other hand, equipotentials for the same rotating spheroid embedded in a thin stationary planar disk can exhibit both a ridge (red) and a groove (green) shown in Figure 2B, and enlarged in Figure 2D. This means that either a ridge or a groove could form depending on the history of material deposition (discussed shortly).

All equipotentials shown are based on a solution to Laplace's equation for a uniform massive ellipsoid that has been known since 1840 (Chasles, 1840). Details of the solution appear elsewhere (Moritz, 1990), and we provide an annotated numerical code for its analysis in Supplementary Materials S1 accompanying this article. The essence of the solution is to break the gravitational geopotential into three parts: a net mass and a quadrupole term that define gravity outside of an ellipsoid of uniform density, and a centrifugal term that accounts for steady

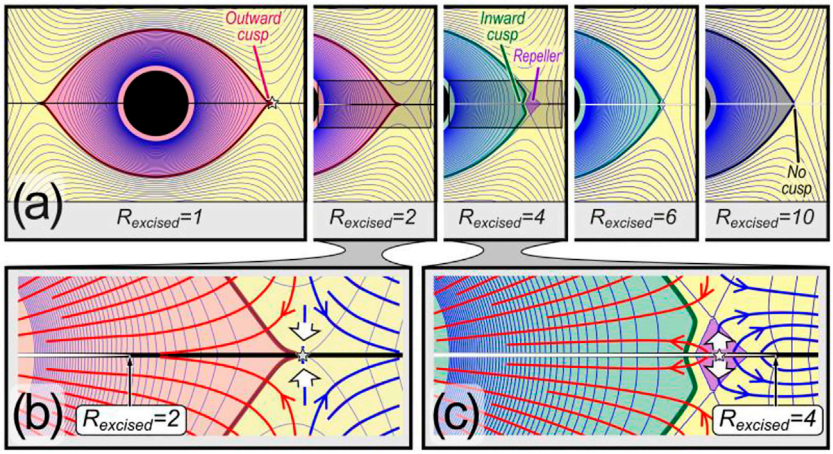

FIGURE 3
Mechanism of bifurcation between outward and inward cusp. **(A)** Progression of cusp shapes as distance, $R_{excised}$, of plane mass from central sphere (black, with radius $R_{polar} = 1$) is increased. **(B)** Enlargement of equipotentials (thin curves) and streamlines (thick curves) for $R_{excised} = 2$. The satellite has an outward cusp (pink, bounded by dark red), and all streamlines move toward the equatorial line in black. Red streamlines indicate that mass is brought toward the satellite and flow toward a single saddle point is indicated by the large white arrows; blue streamlines indicate that mass is taken away from the satellite. **(C)** Equipotentials and streamlines for $R_{excised} = 4$: the white arrows have reversed direction, and all mass within the violet region moves outward, ultimately reaching either the satellite (now green, with an inward cusp) or the plane (black). In all panels, $R_{plane} = 10^2 R_{polar}$, and the plane has thickness $0.02R_{polar}$ as before.

rotation. All terms are 3D, but we take the ellipsoid to have azimuthal symmetry—hence we show 2D cross sections in Figures 2A,B and elsewhere. Surfaces of revolution are included to aid visualization in Figures 1, 5.

In this work we calculate equipotentials of a central spheroid embedded in a planar mass using the geometry sketched in Figure 2C, and we determine shapes of resulting surfaces assuming that deposited mass flows freely with minimal friction. For generality, our analysis defines the central mass rotating at constant angular speed ω, with polar radius R_{polar} and equatorial radius R_{moon}. For simplicity though, unless otherwise specified simulations are for a spherical body ($R_{polar} = R_{moon}$). We superimpose on the central sphere a planar mass that pierces the moon through its equator. It is expected (Charnoz et al., 2007) that mass near a moon will be accreted or expelled over time, so as shown in the figure we excise mass from the plane that lies within a radius $R_{excised}$ surrounding the moon.

We define both the plane and the excised mass using the same 1840 ellipsoidal model as for the central spheroid, but we approximate a planar geometry by using very thin spheroids, with polar radii $0.01R_{moon}$ (i.e., planar thickness $0.02R_{moon}$). The plane has radius R_{plane} much larger than R_{moon}: the value of R_{plane} will be specified in example simulations, but is at least 10 R_{moon} in all cases. The density of the plane, ρ_{plane}, will also be specified: we show results for densities ranging from $\rho_{plane} = 10^{-4}\rho_{moon}$ to $\rho_{plane} = 1.2\rho_{plane}$. In all cases, both the plane and the excised mass have zero angular speed. We take advantage of the fact that Laplace's equation is linear, so that we can obtain the gravitational potential of both the moon and plane by superimposing solutions for each. In order to excise mass from the plane, we simply define the density of the excised region to be negative: $\rho_{excised} = -\rho_{plane}$. The excised region overlaps the plane, so total mass is always non-negative, and varies smoothly from zero at the center of the satellite to ρ_{plane} at the edge of the excised region. Mass is black, and excised region is white in Figures 2, 3.

To summarize, we calculate the gravitational potential, U, as the sum of three parts:

$$U = U_{moon} + U_{plane} + U_{excised} \tag{1}$$

where U_{moon} is the potential for a spinning spheroidal moon with density ρ_{moon}, U_{plane} is the potential of a plane defined to be a stationary spheroid with density ρ_{plane} and thickness 1% that of the moon's equatorial diameter, and $U_{excised}$ is the potential of an excised mass, defined to be a stationary spheroid with negative density, $-\rho_{plane}$, thickness the same as the plane and radius $R_{excised}$ that we will vary. All three bodies are concentric as shown in Figure 2C. Each of the three parts is defined by the 1840 solution in ellipsoidal coordinates; conversions to and from Cartesian coordinates are included in Supplementary Materials S1.

The gravitational potential of a single spheroid has been calculated previously (Hofmeister et al., 2018), but compares unfavorably with shapes of Saturn's moons. The equipotentials shown in Figure 2A are typical, and use $\omega = 15$. Units are nondimensional and chosen for computational convenience, with a gravitational constant $G = 10^4$, and $\rho_{moon} = \frac{3}{4\pi}$, giving the moon unit mass (dimensional comparison for Saturn's moons below).

To examine the effect of a surrounding planar mass, we begin with a first, simplest, example: we consider a central sphere $R_{polar} = R_{moon} = 1$, so that gravitational acceleration at radius r is just $a_{grav} = \frac{-G\,M_{moon}}{r^2}$. This competes against a centrifugal acceleration of $a_{cent} = \omega^2 r$, so $-a_{grav} = a_{cent}$ at the location indicated by the white star in Figure 2A.

The same solution superimposed on a flattened spheroidal plane as we have described is shown in Figure 2B. Parameters for this example are defined in the figure caption; in short, all parameters for the central spheroidal moon are as in Figure 2A, and the

surrounding plane has density half that of the moon: $\rho_{plane} = \frac{1}{2}\rho_{moon}$. The outer radius of the plane is 10 times that of the moon: $R_{plane} = 10R_{moon}$, and the excised radius is chosen to be $R_{excised} = 2.8R_{moon}$ for reasons that we will explain. We discuss next effects of varying each of these parameters; for the time being, we note that both inward and outward cusps arise naturally as equal gravitational potentials of a central moon embedded in a plane as can be seen from the enlargement of Figure 2D.

Two related remarks concerning the equipotentials shown must be stressed before continuing. First, it is important to make clear the meaning of equipotentials. An equipotential is by no means the only possible shape of a satellite: equipotentials are surfaces free of tangential stress, so they are the shapes that would be adopted if surficial material (e.g., freely flowing grains) fully relaxes in response to gravitational and centrifugal forces. Future investigations of accretion history as well as visco-elastic effects, are clearly merited: the intent here is to present shapes that would develop in the freely-flowing limit. Figure 2 shows multiple equipotentials; the choice of which is adopted depends on the amount of mass present. The equipotentials identified in green and red in Figure 2 are chosen to define surfaces with the most pronounced inward or outward cusp respectively. If more material were deposited onto the green surface and allowed to relax freely, the cusp would diminish its curvature, whereas if material were added to the red surface and again allowed to relax freely, it would be stripped away by centrifugal acceleration.

Second, the solutions entirely neglect gravitational interactions between the body and freely flowing material being accreted. These interactions would change the gravitational shape of the body, which in turn would change the shape of the equipotentials, but this fully nonlinear problem is non-integrable, and a complete solution is neither unique nor generally obtainable. We do discuss gravitational influences of a parent body (here, Saturn) at the conclusion of this paper, but we emphasize that the satellite shapes that we display – either with or without Saturn's gravity—are idealized.

With this in mind, to understand the mechanism underlying cusp formation, we observe that cusps emerge as the plane approaches the central spheroid. That is, as $R_{excised} \to R_{plane}$ the effect of the plane vanishes and we recover the cusp-free solution shown in Figure 2A, while as $R_{excised}$ diminishes, the influence of the plane on the moon's gravity grows. So we can examine the effect of the plane by varying $R_{excised}$ between R_{moon} and R_{plane}. This is shown in Figure 3A for the representative case $\omega = 15$ (again, variations in ω will be considered). Parameter values used in Figure 3 are defined in the caption; we have found in multiple trials that the progression shown is quite typical for a wide range of parameter choices.

Figure 3A and the enlargement of Figure 3B show that a nearby concentric plane, $R_{excised} \leq 2$, produces only an outward cusp (seen also in Figures 1E–G). For a more distant plane, $R_{excised} \geq 3$, the outward cusp bifurcates to form an inward cusp and a repeller, highlighted in the enlargement of Figure 3C. Any mass within the region labeled "Repeller" will gravitate either toward the moon or toward the surrounding plane, along the streamlines plotted. Streamlines are defined in the usual way from the potential $U = U_{moon} + U_{plane} + U_{excised}$ defined earlier. As discussed next, the bifurcation of the outward cusp into an inward cusp combined with a repelling region is more intricate than suggested by Figure 3A: evidence of this intricacy is seen in Figure 2B, where we see in a simulation using the same parameters as in Figure 3 that both inward and outward cusps are present between $R_{excised} = 2$ and $R_{excised} = 3$.

Putting details of the bifurcation aside for a moment, the coarse-grained outcome is that if a massive plane is near a satellite, it will tend to produce an outward cusp, and as the planar mass moves away from the moon, the outward cusp will give way to an inward one. As mass recedes still further from the moon, its effect will diminish until equipotentials are indistinguishable from those with no plane at all, shown to the right of Figure 3A at $R_{excised} = 10R_{moon}$.

The mechanism underlying cusp formation can be further exposed by examination of the enlargements of Figures 3B–C. If a massive plane is near the moon, shown in Figure 3B, all nearby mass is drawn equatorward, as the streamlines indicate. This either brings nearby mass toward the moon (red arrows) producing an outward cusp, or brings it away (blue arrows), to augment the surrounding plane. When the plane recedes past the unstable point indicated by the star, a bifurcation reverses mass flow near the starred point. This can be seen by comparing the flow directions shown by the white arrows in Figures 3B,C. This bifurcation arises when the planar mass moves from inside the region identified by the red equipotential in Figures 3A,B (drawing mass inward, toward the moon) to outside that region (drawing mass outward, toward the surrounding plane). Between these two extremes, both states can co-exist, as shown in Figure 2B.

Dynamically speaking, the violet region surrounds what would be the Lagrange point, L1, if there were a single orbiting mass rather than mass within a plane. In our case, for small $R_{excised}$, L1 is a saddle, while for larger $R_{excised}$ the saddle splits in two and L1 becomes an unstable node. This means that an unstable torus devoid of mass can be expected to surround a moon with an inward cusp embedded in a planetary ring (cf. Vesta). We will see shortly that a stable torus is also possible.

In Figure 3 we held ω fixed and varied $R_{excised}$; we next consider effects of varying both ω and $R_{excised}$. This results in Figure 4A, where we plot states near the equator for different values of these parameters. As with Figure 3, this plot is coarse-grained, so it does not detail finer features such as the narrow bistable region that persists at least up to $\omega = 15$ (as shown in Figure 2B). Additionally, we emphasize that the equipotentials shown are obtained through a sequence of computational steps including transforms of coordinates both to and from elliptical coordinates and implicit solutions of a superposition of states for the central ellipsoid and two nearly planar ellipsoids. These calculations (see attached code in Supplementary Material) necessarily have limited accuracy, and as a consequence we report here only unambiguous large-scale features, and disregard smaller-scale intricacies that may or may not be reliable. Our criteria for whether a feature is reliable are whether it changes smoothly with parametric variations, and whether it is larger than observed computational artefacts. For example, the violet repeller shown in Figure 3C grows with both ω and $R_{excised}$, and is seen for other choices of ρ_{plane}. On the other hand, slopes of computational equipotentials near the equator change direction erratically, and so features that never grow above a few percent of R_{polar} are not reported here.

Bearing these caveats in mind, Figure 4 reveals the presence of five distinct states of freely flowing regolith subject to gravitational equipotentials for satellites embedded in a massive plane. For small

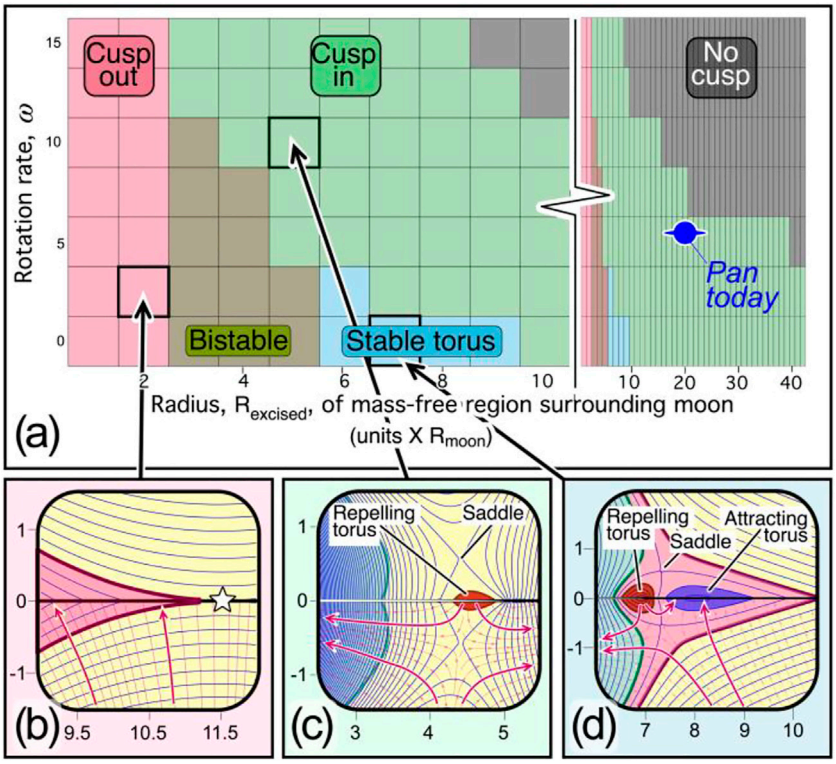

FIGURE 4
Phase diagram of equatorial features of freely flowing material. **(A)** Five distinct states identified as rotation rate ω and central excised mass $R_{excised}$ are varied. Current parameters for the moon Pan are shown for illustrative purposes. Evidently Pan's outward cusps would not form today, and would require disk material much closer than currently seen. **(B–D)** Enlargements of equipotentials and streamlines in cusp regions. Horizontal axes align with disk; axis units agree with those defined earlier, i.e., the central spheroid has radius $R_{polar} = 1$, and the origin is at center of the spheroid. **(B)** For nearby plane (small $R_{excised}$), all mass gravitates equatorward, producing an outward cusp. **(C)** For more distant plane, the bifurcation shown in Figure 3 reverses the flow near a repelling torus, producing an inward cusp. **(D)** For moderate $R_{excised}$ and small ω, a novel attracting torus emerges, bracketed between an inward and an outward cusp; a 3D rendition of the attracting torus appears in Figure 5A. In all panels, $R_{plane} = 10^2 R_{polar}$, and the plane again has thickness $0.02 R_{polar}$.

$R_{excised}$, shown in Figure 4B for $R_{excised} = 2, \omega = 2.5$, an outward cusp is present for any satellite rotational speed, ω. Larger ω values cause material further from the satellite to be centrifuged away: this both reduces the equatorial radius of the equilibrium point at which $a_{grav} = -a_{cent}$ and shortens outward cusps. So elongated outward cusps can be expected at small $R_{excised}$ and small ω, as shown in Figure 4B.

As $R_{excised}$ grows, an inward cusp emerges, shown in Figure 4C for $R_{excised} = 5, \omega = 10$. As we have mentioned, along with this change in cusp direction, a region that repels all mass appears between the satellite and the plane. Between the outward and inward cusp, a third state is possible that supports both cusps. We have already commented briefly on this bistable state, which is shown in Figure 2D for $R_{excised} = 2.8, \omega = 15$. A fourth state arises when the planar mass is far enough away from the central satellite that the inward cusp disappears: in this case, the classical shape shown in Figure 2A is recovered.

Finally, a new, fifth, state is predicted by this model, shown in Figure 4D: for small rotational speeds and for a massive plane around $R_{excised} = 8\, R_{moon}$ away, an attracting region appears through a saddle-node bifurcation. This state is shown in Figure 4D. We note that the repelling and attracting tori should be present for either an inward or an outward cusp, but are unlikely to be observable for an outward cusp since the tori would be inside the satellite's surface. Nevertheless the repelling torus may represent an area of weakness within such a satellite that could cause equatorial mass to break away from its main body. More likely, the attracting state could spontaneously produce a torus around a satellite, and mass injected nearby could become entrained in such a satellite's orbit.

We reiterate that all of these states form for free surface flow under linear and steady-state conditions. History dependence, self-gravitation, and viscoelastic behavior of satellite material are neglected. Processes that generated cusps on Saturn's moons doubtless occurred long ago, and so $R_{excised}$ and ω values in Figure 4 may be useful for evaluating conditions when cusps formed, but are not representative of current conditions.

Nevertheless, we can orient ourselves on Figure 4 using current data, as indicated by the "Pan today" marking in Figure 4A. We have mentioned that units in that panel are dimensionless, and are obtained for a central sphere of unit radius and mass, and a time scale set by choosing the gravitational constant (we use $G_{simulated} = 10^4$ for plotting convenience). For the purpose of orientation, we consider Saturn's moon Pan as an example. Pan lies within the Encke gap, with width 325 km: about 20 times Pan's radius, so

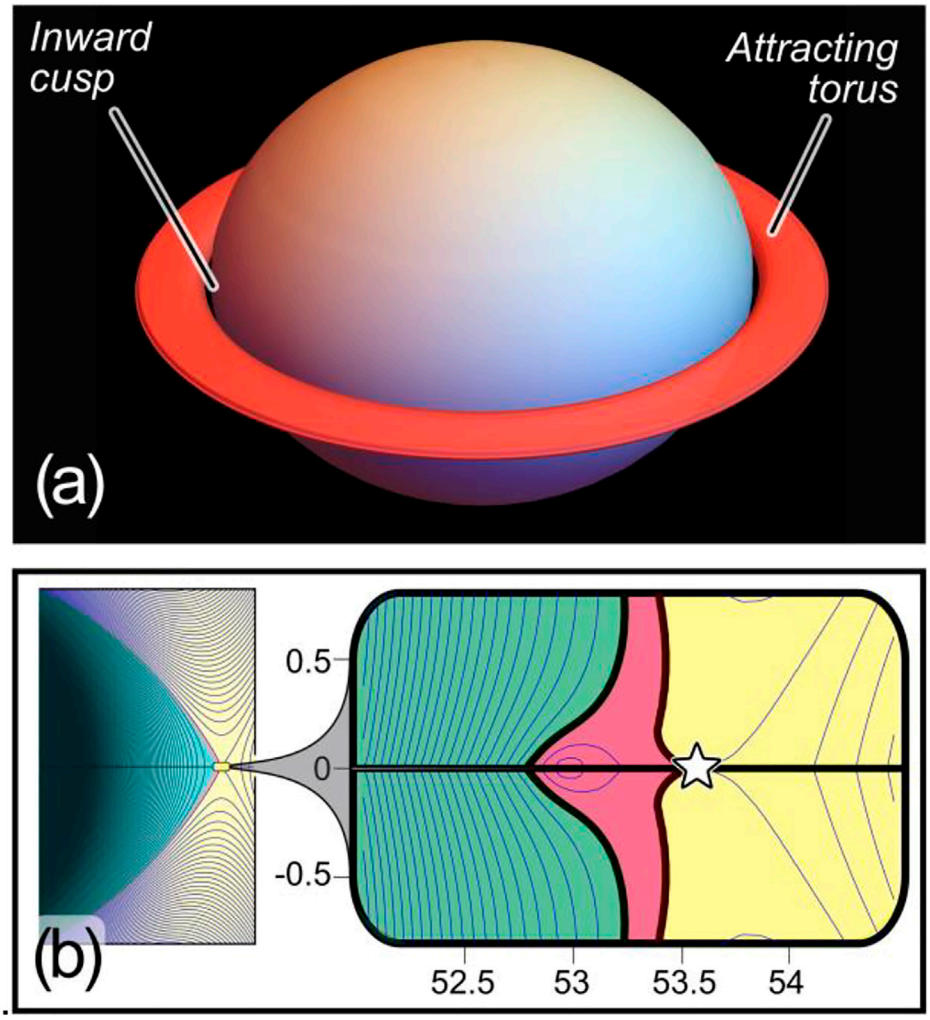

FIGURE 5
Extremes in cusp behavior. **(A)** 3D rendition of attracting torus from Figure 4D. The torus shown is at the outer extreme of the attractive region, and mass would gravitate toward a central torus within. **(B)** Equipotential cusps for very low planar density: $\rho_{plane} = 10^{-4}\rho_{moon}$; axis units as in Figure 4. Left panel shows equipotentials to right of the attracting body; right panel shows enlargement, including both inward (green) and outward (red) cusps, as well as equal force point identified by star. Parameters are $R_{plane} = 10^3 R_{polar}$, $R_{excised} = 53R_{polar}$, $\omega = 0.25$, and central mass is a sphere and the plane again has thickness $0.02R_{polar}$.

$R_{excised}$ is at least 20 currently. Pan has density $\rho = 420$ kg/m^3 and is tidally locked with frequency $\omega = 2{\cdot}10^{-5}$ sec^{-1}, which we can relate to the ordinate in Figure 4 by making use of the dimensionless group, $\mathcal{G} = \frac{G{\cdot}\rho}{\omega^2} = \frac{6.7{\cdot}10^{-11}{\cdot}420}{2{\cdot}10^{-5^2}} = 70$. Applying the same dimensionless group to our simulations, $\mathcal{G} = 70 = \frac{G_{simulated}{\cdot}\rho_{simulated}}{\omega^2_{simulated}} = \frac{10^4{\cdot}0.24}{\omega^2_{simulated}}$, so the corresponding simulated frequency is $\omega_{simulated} \sim 6$, at the location shown in Figure 4A.

In Figure 5A, we also plot the stable torus' location for the conditions shown in Figure 4D: $R_{excised} = 7, \omega = 0$, and $\rho_{plane} = \frac{1}{2}\rho_{moon}$, $R_{plane} = 100R_{polar}$ (the parameters used in the other cases shown in Figures 3, 4). The image in Figure 5A displays the outside of the attracting torus: freely flowing material will gravitate toward a small region at its center; moreover we emphasize that tidal perturbations and debris impacts can remove this material, and the torus will become unstable as the planar mass recedes. Nevertheless, straightforward analysis of equipotentials indicates that a stable torus ought to be present in some satellites within a planetary ring. Interestingly, this torus appears at small—even zero—angular speed ω, thus material in the torus can rest stably without orbital velocity!

Two final, practical, issues remain. First, arguably the mass of Saturn's disk material could seem to be too small to produce significant gravitational effects on its moons, and second, effects of Saturn's gravity (mentioned earlier) are yet to be discussed. We consider these two issues next.

Saturn's disk mass

With respect to the mass of Saturn's disk material, two facts suggest that this mass could be sufficient to produce the satellite shapes that we have displayed. First, the density of Saturn's rings was

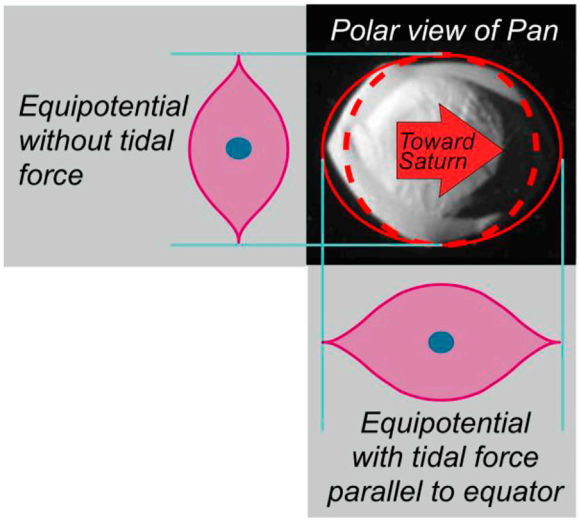

FIGURE 6
Pan and orthographic depictions of distortion of gravitational equipotentials by tidal force from distant planet. Upper right shows polar view of Pan with superimposed circle (dashed curve) and ellipse (solid). The ellipse's semi-minor axis is obtained from the maximum radius of potential (Thomas et al., 2015); cross-section shown in upper left. The ellipse's semi-major axis is obtained by adding the potential (Shinbrot et al., 2004) with $\vec{r}_{moon}$ aligned with the horizontal, with a convenient magnitude of the maximum tidal acceleration. Other magnitudes are included in the Supplementary Materials. Pan credit: NASA/JPG-Caltech/SSI.

almost certainly higher during the evolution of its moons than it is today (Charnoz et al., 2007). Indeed, prior work (Salmon and Canup, 2017) has estimated the ratio of the mass of rings to moons to have been as high as 1:3. By the same token, satellites (e.g., Iapetus) or asteroids (e.g., Vesta) that are currently far from disk material may have been embedded in such material earlier during their formation. Second, we can quantify how large the density of a surrounding plane must be to produce equatorial cusps, and we will next show that cusps arise even for extremely small planar densities.

To evaluate effects of planar density, ρ_{plane}, we perform an additional set of simulations holding ρ_{moon} fixed and reducing ρ_{plane} by successive orders of magnitude to determine the point at which cusps vanish. Specifically, at each value of ρ_{plane}, ranging from $\rho_{plane} = \rho_{moon}$ to $\rho_{plane} = 10^{-5}\rho_{moon}$, we manually adjust $R_{excised}$ and ω to determine whether cusps are present. This is easily done by making use of the facts first that cusps are stabilized by reducing ω (which reduces centrifugal stripping of material from the cusp) and second that cusps tend toward higher $R_{excised}$ at smaller ω (cf Figure 4). So by examining equipotentials near the starred equilibrium point while incrementally reducing ω and increasing $R_{excised}$, cusps are readily identified.

From this exercise, we find that cusps persist at least down to $\rho_{plane} = 10^{-4}\rho_{moon}$. We show both inward and outward cusps in Figure 5B for this case: these appear with the plane held at a distance, $R_{excised}$, over 50 times the central mass' radius, and for very small rotation rate. Even smaller cusps may be present at lower planar densities, but they are at most a few percent of R_{polar} in size, and as we have mentioned this is the same size as computational noise and so are disregarded here. Ultimately we conclude that even planar disk densities 1/10,000th that of a central spheroid—and at a distance 50 times the radius of the central mass—are sufficient to produce equatorial cusps in gravitational equipotentials. By comparison, the moons Pan and Atlas have densities estimated (Porco et al., 2007) to be 410–450 kg/m^3, while recent calculations (Iess et al., 2019) indicate that the densities of Saturn's rings range from zero up to 60 kg/m^3: a difference of about 1/10.

It remains uncertain how dense the rings once were, but comparison with the 1/10,000 figure that produces cusps suggests that sufficient ring density may be present, even currently, to affect satellite geomorphology. Moreover as we have mentioned, the observation that a interplanetary body is currently far from a planar mass does not imply that the body was not influenced by such a mass earlier in its history. Since it is not possible to determine complete histories of these bodies in retrospect, we propose that their current morphologies can be used to provide evidence of that history *a posteriori*. That is, on mathematical grounds, we find that circumferential ridges and grooves on celestial bodies may be indications that the bodies at one time were embedded in a planar mass and covered with freely flowing regolith.

Saturn's gravity

This brings us to the final practical issue: effects of Saturn's gravity. Here we note that Saturn's gravity at the current locations of Pan and Atlas is 3 orders of magnitude stronger than their surface gravities. From that perspective, the relevance of analyzing gravitational equipotentials needs justification.

Pan and Atlas are currently about $R_{orbital} = 1.3 \cdot 10^8$ m from Saturn, and are maintained in orbit by outward centrifugal acceleration. Explicitly, at that distance, the net inward acceleration acting on a moon in a circular orbit is:

$$a_{moon} = \frac{G\,M_{Saturn}}{R_{orbital}^2} - \frac{v^2}{R_{orbital}} \tag{2}$$

where G is the universal gravitational constant, M_{Saturn} is Saturn's mass, and v is the moon's orbital speed, all of which are known. At equilibrium, a_{moon} at a moon's center of mass is zero, while the difference in acceleration from the near to the far side of a moon with radius r_{moon} is given by:

$$\Delta a_{moon} = \left(-\frac{2G\,M_{Saturn}}{R_{orbital}^{\ 3}} + \frac{v^2}{R_{orbital}^{\ 2}} \right) 2r_{moon} \tag{3}$$

This is the maximum acceleration responsible for tides (Chandrasekhar, 1989), and is readily evaluated. For the four examples shown in Figure 1, from right to left, Vesta is not in Saturn's orbit, and both a_{Vesta} and Δa_{Vesta} are zero. So if Vesta were in a massive plane far from a central body earlier in its history (which is not known), the equipotentials presented earlier could be obtained. Iapetus is very massive and is currently far from Saturn than Iapetus, so $\Delta a_{Iapetus}$ is small: under 10^{-4} times its surface gravity, and again there is justification for neglecting the mass of a central body. Pan and Atlas, on the other hand, are both less massive and closer to Saturn than Iapetus Δa_{Pan} and Δa_{Atlas} are respectively about 1/4 and 1/5 of the moon's surface gravity.

Focusing on these two moons that are most strongly influenced by Saturn's gravity, Atlas' rotation rate is not known, but Pan is in synchronous rotation with the same side always facing Saturn, so tidal forcing on its surface is static and its perturbation to the equipotential due to Saturn is bounded by the following term:

$$U_{tidal} = -\int \Delta a_{\text{moon}}\, d\vec{r}_{moon} \tag{4}$$

where $\vec{r}_{moon}$ points toward Saturn. Adding this to the potential, Eq. 1 provides us with an idealized potential from a perturbation due to Saturn's gravity.

In Figure 6, we plot a polar photograph of Pan alongside orthographic views of the deformation that one would naïvely obtain from Eq. 4. The superimposed dashed line in the polar view is a simple circular outline, as would be expected without a perturbing gravitational potential. The solid line shows an ellipse with semi-minor axis of the circle and semi-major axis obtained by adding the perturbation of Eq. 4. The arrow indicates Pan's orientation with respect to Saturn, and the orthographic views give respective cross-sections that one would expect perpendicular to (i.e., uninfluenced by) Saturn's field, and parallel to Saturn's gravity.

This is again only an idealized analysis and is far simpler than the complete problem—for example, both the temporal reshaping due to long periods of tidal damping and important nonlinear interactions are overlooked. Likewise, continuing the spirit of the rest of our analysis, we neglect changes to equipotentials due to redistribution of mass, here from the orbital direction to the Saturn-moon direction. The merit of Eq. 1 and Eq. 4 is that they permit us to calculate equipotentials, which give the lowest order stress-free state of a satellite's surface that could be expected to be adopted by a linear analysis of individual and sedately settling particles.

Conclusion

It is well recognized that Saturn's moons affect its rings (Pollack, 1975), for example, producing wakes, gaps and resonances that dominate ring morphology (Showalter et al., 1986). Effects that rings have on moons are less well studied (Charnoz et al., 2007), and gravitational potentials of satellites are assumed to be insensitive to influences of rings. Contrary to this assumption, we have found that distinctive features of Saturn's moons, including equatorial cusps and even a predicted stable circumferential torus, arise naturally by including the influence of rings in the simplest possible gravitational model of a central satellite surrounded by a massive equatorial plane. Remarkably, equatorial cusps endure even for distant and low mass rings. It is important to emphasize that these results are purely linear: like the effect that moons have on rings, we neglect nonlinear feedback between rings and moons. It is likely—especially since ring densities several orders of magnitude smaller than moon density have significant gravitational effects—that this feedback is important, and indeed the model presented here does not yet consider how accreted mass affects a satellite's gravitational potential. A fully nonlinear model continues to be an important challenge. Likewise, as we have mentioned, results here apply in the limit of entirely freely flowing grains: effects of accretion history and of friction, viscosity, and elasticity also remain for future investigation.

Data availability statement

The original contributions presented in the study are included in the article/Supplementary Material, further inquiries can be directed to the corresponding author.

Author contributions

The author confirms being the sole contributor of this work and has approved it for publication.

Funding

This material is based on support from NSF CBET, Award No. 1804286.

Conflict of interest

The author declares that the research was conducted in the absence of any commercial or financial relationships that could be construed as a potential conflict of interest.

Publisher's note

Supplementary material

The Supplementary Material for this article can be found online at: https://www.frontiersin.org/articles/10.3389/fspas.2023.1146705/full#supplementary-material

References

Buratti, B. J., Thomas, P. C., Roussos, E., Howett, C., Seiss, M., Hendrix, A. R., et al. (2019). Close cassini flybys of Saturn's ring moons Pan, Daphnis, Atlas, Pandora, and epimetheus. *Science* 364, eaat2349. doi:10.1126/science.aat2349

Chandrasekhar, S. (1989). The equilibrium and the stability of the roche ellipsoids: lasma physics, hydrodynamic and hydromagnetic stability, and applications of the tensor-virial theorem. *Sel. Pap.* 4, 430.

Charnoz, S., Brahic, A., Thomas, P. C., and Porco, C. C. (2007). The equatorial ridges of Pan and Atlas: Terminal accretionary ornaments? *Science* 318 (5856), 1622–1624. doi:10.1126/science.1148631

Charnoz, S., Crida, A., Castillo-Rogez, J. C., Lainey, V., Dones, L., Karatekin Ö, Tobie G., et al. (2011). Accretion of Saturn's mid-sized moons during the viscous spreading of young massive rings: Solving the paradox of silicate-poor rings versus silicate-rich moons. *Icarus* 216 (2), 535–550. doi:10.1016/j.icarus.2011.09.017

Chasles, M. (1840). "Solution nouvelle du problème de l'attraction d'un ellipsoïde hétérogène sur un point exterieur," Jour. *Liouville* 5, 465–488.

Hofmeister, A. M., Criss, R. E., and Criss, E. M. (2018). Verified solutions for the gravitational attraction to an oblate spheroid: Implications for planet mass and satellite orbits. *Planet. Space Sci.* 152, 68–81. doi:10.1016/j.pss.2018.01.005

Iess, L., Militzer, B., Kaspi, Y., Nicholson, P., Durante, D., Racioppa, P., et al. (2019). Measurement and implications of Saturn's gravity field and ring mass. *Science* 364, eaat2965. doi:10.1126/science.aat2965

Lauretta, D. S., Balram-Knutson, S. S., Beshore, E., Boynton, W. V., Drouet d'Aubigny, C., DellaGiustina, D. N., et al. (2017). OSIRIS-REx: Sample return from asteroid (101955) bennu. *Bennu. Space Sci. Rev.* 212 (1), 925–984. doi:10.1007/s11214-017-0405-1

Leleu, A., Jutzi, M., and Rubin, M. (2018). The peculiar shapes of Saturn's small inner moons as evidence of mergers of similar-sized moonlets. *Nat. Astron.* 2 (7), 555–561. doi:10.1038/s41550-018-0471-7

Meakin, P., Ramanlal, P., Sander, L. M., and Ball, R. C. (1986). Ballistic deposition on surfaces. *Phys. Rev. A* 34 (6), 5091–5103. doi:10.1103/physreva.34.5091

Moritz, H. (1990). The figure of the earth: Theoretical geodesy and the earth's interior. *Karlsr. Wichmann*, pp.126–60.

Pollack, J. B. (1975). The rings of Saturn. *Space Sci. Rev.* 18 (1), 3–93. doi:10.1007/bf00350197

Porco, C. C., Thomas, P. C., Weiss, J. W., and Richardson, D. C. (2007). Saturn's small inner satellites: Clues to their origins. *science* 318 (5856), 1602–1607. doi:10.1126/science.1143977

Salmon, J., and Canup, R. M. (2017). Accretion of Saturn's inner mid-sized moons from a massive primordial ice ring. *Astrophysical J.* 836 (1), 109. doi:10.3847/1538-4357/836/1/109

Shinbrot, T., Duong, N. H., Kwan, L., and Alvarez, M. M. (2004). Dry granular flows can generate surface features resembling those seen in Martian gullies. *Proc. Natl. Acad. Sci.* 101 (23), 8542–8546. doi:10.1073/pnas.0308251101

Shinbrot, T., Sabuwala, T., Siu, T., Lazo, M. V., and Chakraborty, P. (2017). Size sorting on the rubble-pile asteroid Itokawa. *Phys. Rev. Lett.* 118 (11), 111101. doi:10.1103/physrevlett.118.111101

Showalter, M. R., Cuzzi, J. N., Marouf, E. A., and Esposito, L. W. (1986). Satellite "wakes" and the orbit of the Encke Gap moonlet. *Icarus* 66 (2), 297–323. doi:10.1016/0019-1035(86)90160-0

Thomas, N., Sierks, H., Barbieri, C., Lamy, P. L., Rodrigo, R., Rickman, H., et al. (2015). Cometary science. The morphological diversity of comet 67P/Churyumov-Gerasimenko. *Science* 347, aaa0440. doi:10.1126/science.aaa0440